

The Structure of Solar Coronal Mass Ejections in the Extreme-Ultraviolet Passbands

H. Q. Song¹, J. Zhang², L. P. Li³, Y. D. Liu⁴, B. Zhu⁴, B. Wang¹, R. S. Zheng¹, and Y. Chen¹

1 Shandong Provincial Key Laboratory of Optical Astronomy and Solar-Terrestrial Environment, and Institute of Space Sciences, Shandong University, Weihai, Shandong 264209, China

`hqsong@sdu.edu.cn`

2 Department of Physics and Astronomy, George Mason University, Fairfax, VA 22030, USA

3 Key Laboratory of Solar Activity, National Astronomical Observatories, Chinese Academy of Sciences, Beijing, 100101, China

4 State Key Laboratory of Space Weather, National Space Science Center, Chinese Academy of Sciences, Beijing, 100190, China

ABSTRACT

So far most studies on the structure of coronal mass ejections (CMEs) are conducted through white-light coronagraphs, which demonstrate about one third of CMEs exhibit the typical three-part structure in the high corona (*e.g.*, beyond $2 R_{\odot}$), *i.e.*, the bright front, the dark cavity and the bright core. In this paper, we address the CME structure in the low corona (*e.g.*, below $1.3 R_{\odot}$) through extreme-ultraviolet (EUV) passbands and find that the three-part CMEs in the white-light images can possess a similar three-part appearance in the EUV images, *i.e.*, a leading edge, a low-density zone, and a filament or hot channel. The analyses identify that the leading edge and the filament or hot channel in the EUV passbands evolve into the front and the core later within several solar radii in the white-light passbands, respectively. What's more, we find that the CMEs without obvious cavity in the white-light images can also exhibit the clear three-part appearance in the EUV images, which means that the low-density zone in the EUV images (observed as the cavity in white-light images) can be compressed and/or transformed gradually by the expansion of the bright core and/or the reconnection of magnetic field surrounding the core during the CME propagation outward. Our study suggests that more CMEs can possess the clear three-part structure in their early eruption stage. The nature of the low-density zone between the leading edge and the filament or hot channel is discussed.

Subject headings: Sun: coronal mass ejections (CMEs) – Sun: prominences – Sun: activity

1. Introduction

Coronal mass ejections (CMEs) are one of the most energetic explosions in the solar atmosphere, which can release large quantities of magnetized plasmas, magnetic fluxes, and energetic particles into the interplanetary space (Forbes et al. 2006; Chen 2011; Webb & Howard 2012), and produce geomagnetic storms that may adversely impact human high-technology systems around the Earth (e.g., Gosling et al. 1991; Webb et al. 1994, 2000; Zhang et al. 2003, 2007). Theoretically, CMEs result from the eruption of magnetic flux ropes (MFRs), whenever the ropes are formed prior to (Chen 1996; Lin & Forbes 2000; Lin et al. 2004) or during (Mikić & Linker 1994; Antiochos et al. 1999) the eruptions. MFR is a coherent magnetic structure with magnetic field lines wrapping around its central axis, *i.e.*, its field lines exhibiting obvious twist (e.g., twist number > 1). There is no physical mechanism that can produce a CME from the corona without involving an MFR. Observationally, CMEs are usually associated with the eruption of filaments (*i.e.*, prominences when located near the solar limb, Webb & Hundhausen 1987; Gopalswamy et al. 2003) or hot channels (Nindos et al. 2015; Zhang et al. 2015). Filaments are dense and cold materials trapped at the MFR dips, *i.e.*, sites where the field lines are locally horizontal and curved upward (Kippenhahn & Schlüter, 1957). Hot channels refer to the high-temperature coronal structure revealed in the 131 or 94 Å passbands (Zhang et al. 2012), and they can appear as the hot blobs if observed along their axis due to the projection effect (Cheng et al. 2011; Song et al. 2014a, 2014b). Many researches support that the hot channels act as the proxy of MFRs (Zhang et al. 2012; Patsourakos et al. 2013; Cheng et al. 2014; Song et al. 2015). Therefore, the eruption of MFRs in theories usually manifests as the ejection of filaments or hot channels in observations.

Understanding various aspects of CMEs is of important significance, among which one basic issue is their structure that provides a crucial clue to investigate the eruption process. A recent statistical study classified CMEs into five categories based on their appearance characteristics in the white-light coronagraphic images (Vourlidas et al. 2013), including the three-part structure (CMEs with a bright front, a dark cavity, and a bright core), loop (CMEs with a bright loop but lacking a cavity and/or a core), jet (narrow CMEs with angular width less than 40 degrees), outflow (CMEs wider than jets, without clear loop front or cavity), and failed (CMEs that disappear in the outer corona). The three-part structure has been considered as the archetypical configuration in the research field, though previous studies revealed that only about one third of CMEs possess this appearance (e.g., Illing & Hundhausen 1985). Song et al. (2017) demonstrated that at least two factors can reduce the probability of CMEs exhibiting the three-part structure, including the observational time or altitude (evolution effect) and perspective (projection effect). They claim that more three-part CMEs could be observed in the early stage of CME eruptions (*viz* in the low corona) and/or with suitable observational viewpoint. To further examine the validity of these claims is our first motivation to investigate the CME structure in the low corona through EUV passbands.

As the brightness in white-light coronagraphs is proportional to the electron column density (e.g., Hayes et al. 2001), the three-part structure corresponds to a high-low-high density sequence.

When the MFR, with dense filament located in its trailing part, lifts off from the source region, it will expand and compress its overlying loops successively (e.g., Chen 2009), then the background plasmas can pile up along the MFR front border and evolve into the CME bright front (Forbes, 2000). Therefore, the three-part structure of CMEs has been explained as the manifestations of coronal plasma pileup (high density), MFR (low density), and filament (high density) sequentially for several decades. Recently, the interpretation of the CME core is challenged (Howard et al. 2017; Song et al. 2017). Howard et al. (2017) conducted a survey based on 42 CMEs all with the three-part structure, which illustrated that $\sim 69\%$ of the events are not associated with any eruptive filament. They speculated that the CME core is produced by the geometric projection of a twisted MFR. Song et al. (2017) clearly demonstrated that the hot channel MFR corresponds to the bright core through a filament-unrelated CME from both edge-on and face-on perspectives. Therefore, both the filament and MFR (e.g., hot channel) can be observed as the CME core in the coronagraphs. Song et al. (2019) further presented a three-part CME with both a sharp and a fuzzy core, which correspond to the filament and the MFR, respectively. Since the MFR may appear as the CME core in the new scenario, one key question arises naturally, *i.e.*, what is the nature of the CME cavity in the white-light images? It might correspond to different part of the MFR due to projection effect (e.g., Howard et al. 2017). Alternatively, the cavity might be just a low-density zone without helical fields (Song et al. 2017, 2019). To shed more light on this issue is our second motivation to investigate the CME structure in the EUV passbands.

The white-light coronagraphs capture the Thomson-scattered light from the free electrons in the corona, which is dependent on the electron density as mentioned, while the EUV passbands are dependent on both the density and temperature of the coronal plasma (e.g., Del Zanna & Mason 2018). In the meantime, the white-light intensities are more sensitive to coronal features near the plane of sky (POS, e.g., Vourlidis & Howard 2006), while the EUV passbands are less preferentially sensitive to features based on their locations relative to the POS. Therefore, the density structures in the white-light and the EUV passbands can be compared and correlated each other more straightforwardly for limb CMEs. We select four CMEs originating near the limb in this paper, including two (two) events with (without) the obvious cavity in the coronagraphs, which are associated with the eruption of a filament and a hot channel, respectively. The instruments are introduced in Section 2, and the observations and results are presented in Section 3. Section 4 is our summary, which is followed by discussions in Section 5.

2. Instruments

The EUV data sets are provided by three instruments, including the Atmospheric Imaging Assembly (AIA; Lemen et al. 2012) on board the *Solar Dynamics Observatory (SDO)*, the Extreme Ultraviolet Imager (EUVI; Howard et al. 2008) on board the *Solar Terrestrial Relations Observatory (STEREO)*, as well as the Solar Ultraviolet Imager (SUVI; Seaton & Darnel 2018) on board the *GOES-16*. The white-light coronagraphs COR1 (Howard et al. 2008) on board the *STEREO*, and

the Large Angle and Spectrometric Coronagraph (LASCO; Brueckner et al. 1995) on board the *Solar and Heliospheric Observatory (SOHO)* are used to analyze the CME structure in the high corona. The *SOHO*, *SDO*, and *GOES-16* observe the Sun from the Earth viewpoint. The *STEREO* consists of twin spacecraft orbiting the Sun, one ahead of (A) and the other behind (B) the Earth, which can provide observations from different perspectives as each one separates from the Earth by $\sim 22^\circ$ every year in heliocentric longitude.

The AIA records the low corona with the FOV (field of view) of $1.3 R_\odot$, cadence of 12 s and resolution of $0.''6$ per pixel in seven EUV passbands. The SUVI images the solar corona with an FOV larger than $1.6 R_\odot$ in the horizontal direction in six EUV passbands. The EUVI provides the solar EUV images at four wavelength with an FOV of $1.7 R_\odot$, partially overlapping with that of COR1 ($1.4\text{--}4 R_\odot$), which enables us to observe the object continuously from the solar surface to the outer corona. The LASCO possesses an FOV covering $2.2\text{--}30 R_\odot$ (C2: $2.2\text{--}6 R_\odot$; C3: $4\text{--}30 R_\odot$).

3. Observations and Results

3.1. Two CMEs with Obvious Cavity

In this subsection, two CMEs with typical three-part structure in the white-light images are analyzed. One occurred on 2013 September 24, associated with a filament eruption, and the other erupted on 2015 February 9, associated with a hot channel eruption.

3.1.1. The 2013 September 24 Event

A CME was recorded by the LASCO on 2013 September 24 as shown in Figure 1(a1), which exhibits a clear and typical three-part structure. The CME first appeared in the C2 FOV at 20:36 UT and propagated outward at a linear speed of 919 km s^{-1} (CDAW: <https://cdaw.gsfc.nasa.gov/>) near the Sun. Through inspecting the SDO/AIA observations, we can correlate this CME with a filament eruption unambiguously. Figure 1(a2) presents one snapshot of the filament eruption provided by the AIA running-difference image at 193 \AA wavelength, which demonstrates that the event already possesses the three-part appearance in the early stage, *i.e.*, the leading edge as marked with blue dots, the filament as denoted with the red arrow, and a zone between them can be distinguished. Please see the accompanying animation to examine the eruption process in the EUV passband.

The *STEREO-B* is $\sim 139^\circ$ east of the Earth during this eruption. Both the EUVI B and COR1 B record the CME and its source region. Figure 2(a) presents the EUVI B 195 \AA running-difference image at 20:16 UT, which also displays the three-part appearance with the blue and red dots depicting the leading edge and filament, respectively. These dots are replotted in the COR1

image as shown in Figure 2(b). It is straightforward that the leading edge in the EUV passband corresponds to the CME front in the white-light coronagraph. At 20:16 UT, the filament as denoted with the red dots is still blocked by the occulter as shown in Figure 2(b), hence no CME core is observed by the COR1 B at this time. Twenty minutes later, the filament ascends to a higher altitude as presented in Figure 2(c). The filament front is depicted with red dots again and the dots are superimposed on the COR1 image recorded at the same time (Figure 2(d)), which clearly demonstrates that the filament corresponds to the CME core. A similar situation was obtained by overlapping EUVI and COR1 (Liu et al. 2010; Liu et al. 2014). Therefore, we conclude that the leading edge and filament observed in the EUV passband evolve into the bright front and core of three-part CME in the white-light images. Naturally, the zone between the leading edge and the filament should evolve into the dark cavity of the CME in the white-light images, illustrating the zone with lower density. Note the cyan squares in the right panels depict the FOV of left panels.

3.1.2. The 2015 February 9 Event

Another CME with the typical three-part structure occurred on 2015 February 9 and was recorded by the LASCO as displayed in Figure 1(b1). The CME first appeared in the C2 FOV at 23:24 UT and moved outward at the linear speed of 1106 km s^{-1} (CDAW) in the LASCO FOV. After inspecting the observations of LASCO and AIA, we can correlate this CME with a hot channel eruption. Figure 1(b2) is a composite observation of AIA 193 Å running-difference image (gray) and 131 Å direct image (cyan). The leading edge (193 Å) and the hot channel (131 Å) are depicted with blue and red dots, respectively, which shows that a zone exists between the leading edge and the hot channel. Please check the accompanying animation to observe the three-part configuration in the EUV passbands clearly. As the hot channel density is higher than its surrounding environment as revealed by the differential emission measure analysis (Cheng et al. 2012), *i.e.*, the zone density is lower compared to both the hot channel and the piled-up leading edge. Therefore, for this CME induced by the hot channel eruption, we also believe that the three-part configuration in the EUV images evolves into the three-part structure in the white-light images correspondingly, which means the hot channel evolves into the bright core of the CME as suggested in Song et al. (2017).

3.2. Two CMEs without Obvious Cavity

In this subsection, we analyze two CMEs without obvious cavity existing between the front and core in the white-light images, which are also associated with the eruptions of a filament and a hot channel, respectively. One occurred on 2014 January 6, and the other on 2017 September 10.

3.2.1. The 2014 January 06 Event

The LASCO recorded a CME on 2014 January 6 that first appeared in the C2 FOV at 08:00 UT and moved in the coronagraphic FOV at a linear speed of 1402 km s^{-1} (CDAW). The CME does not exhibit the clear three-part structure in the white-light image as no obvious dark cavity can be distinguished as displayed in Figure 3(a1). One interesting phenomenon is that the CME front exhibits a local deformation, *i.e.*, a bulge appears at the front as denoted with the yellow arrow, which can be observed more clearly in the running-difference image (Figure 3(a2)).

The *STEREO-B* is $\sim 153^\circ$ east of the Earth during this eruption. Through inspecting both the white-light and EUV observations, the source region can be identified unambiguously. The CME results from a filament eruption that is recorded by the AIA and EUVI B simultaneously from two viewpoints. Figure 3(a3) presents the AIA 193 Å running-difference image, demonstrating the three-part appearance, *i.e.*, the leading edge, the filament as denoted with the red arrow, and the zone between them. The EUVI B 195 Å observation presents the similar result as shown in Figure 3(a4), where the filament is depicted with the red arrow. The leading edge, the filament and the zone between them in the EUV images (panel (a3)) should evolve into the bright front, bright core and dark cavity in the white-light images, respectively. However, no obvious dark cavity is recorded in the coronagraph as shown in panel (a1). This will be discussed later with the next event together.

3.2.2. The 2017 September 10 Event

This event was recorded by the *SOHO* and *STEREO-A* from two perspectives on 2017 September 10 when the *STEREO-A* was 128° east of the Earth, which was accompanied by an X8.2 class flare and has been used to investigate various aspects of CMEs (Yan et al. 2018; Veronig et al. 2018 and references therein). The CME first appeared in the C2 FOV at 16:00 UT at a high linear speed of 3163 km s^{-1} (CDAW). The LASCO observation shows that the CME does not possess the obvious dark cavity either as displayed in Figure 3(b1). The CME front also exhibits a bulge as depicted with the yellow arrow, which is more distinguishable in the running-difference image (Figure 3(b2)).

Through inspecting the LASCO and AIA observations, we can find the source region without ambiguity. Figure 3(b3) presents the AIA 131 Å observations, clearly showing that the CME is driven by the eruption of a hot blob. Due to the AIA limited FOV, partial blob and the leading edge are not imaged by the AIA at 15:55:30 UT. We acquire the blob outline based on the observation at 15:55:06 UT as marked with red dots in the inset panel, assuming that the blob does not change its morphology significantly. At the same time, the leading edge can be observed clearly in the SUVI FOV through the 195 Å passband as shown in Figure 3(b4), where the hot blob outline recorded by the AIA is replotted with red dots. This figure clearly demonstrates that the CME also possesses the three-part appearance in the EUV passbands. The bulge is formed in the propagation direction

of the expanding hot blob, which moves much faster than the CME front, and thus protrudes from the bottom of the CME front (Veronig et al. 2018). This illustrates the low-density zone in the low corona can be compressed significantly during propagation outward.

Figure 4(a) displays the EUVI A 195 Å observation at 15:58 UT, only showing the leading edge as depicted with the blue dots. Since the hot blob temperature is very high (beyond 10 MK, see Cheng et al. 2018), it is unobservable in the 195 Å passband. Please check the accompanying animation to examine the eruption in the EUV passband. However, the high density characteristics of both the leading edge (blue dots) and the hot blob (red dots) can be revealed by the COR1 observation simultaneously as shown in Figure 4(b) after they entered into the COR1 FOV at 16:05 UT. Note the central part of the bright front is not clear enough to be identified in the static image, please check the animation for the continuous observations in the white-light passband. This demonstrates again that the leading edge and the hot blob evolve into the bright front and the core of CME, respectively.

Figure 5 presents six running-difference images recorded by the LASCO/C3. The bulge at the CME front keeps obvious as denoted with the yellow arrow in each panel, and locates in the propagation direction of the expanding core as depicted with the red arrows. In the meantime, as the CME expansion speed decreases over time (Liu et al. 2019), the separation between the driven shock and the CME front appeared gradually at both flanks of the CME as depicted with the blue arrows. This phenomenon has been reported in the EUV passband (Cheng et al. 2012), demonstrating that the EUV leading edge can contain two components, i.e., the pile-up plasma (corresponding to the bright front of CME in the coronagraphs) and the EUV wave (or shock when the CME speed is high enough).

4. Summary

In this paper, we selected four limb events to study the CME structure at their initial eruption stage through the EUV passbands. The observations demonstrated that all the four CMEs can possess the three-part appearance in the EUV images, wherever they were associated with the eruption of a filament or a hot channel MFR, and whether they had obvious cavity or not in the white-light images. If the three-part appearance in the low corona observed through the EUV passbands can be imaged by the coronagraphs at the same time, the white-light data will also record a three-part CME with the obvious cavity. Our study further confirmed that both the filament and the hot channel can appear as the bright core of CMEs in the coronagraphs. Our observations illustrated that the low-density zone (dark cavity) can decrease gradually in size (Subsection 3.2) when the CME propagates outward due to the core expansion and/or reconnection, which obscures or eliminates the three-part structure in the high corona. Therefore, we suggest that more CMEs (not only about one third as usually cited) possess the typical three-part structure in the low corona (e.g., below $1.3 R_{\odot}$). This is consistent with the cavity surveys in both EUV and white-light passbands, which demonstrated that nearly 80% of the surveyed days had one or more EUV

cavity (Forland et al. 2013), versus 10% of the white-light days surveyed (Gibson et al. 2006). More comprehensive statistics should be conducted to get the exact percentage of the three-part CMEs in the low corona.

5. Discussions on the Nature of the Low-density Zone (Dark Cavity)

Based on the traditional explanation of the three-part structure of CMEs, *i.e.* the bright core and the dark cavity correspond to the filament and the MFR, respectively, the MFR will expand and the cavity volume should increase correspondingly during the propagation, instead of decreasing as observed in Subsection 3.2. On the other hand, based on the new scenario of the CME three-part structure, in which the bright core and the dark cavity correspond to the MFR and the low-density zone, respectively, it is straightforward to understand the decrease of the dark cavity volume. Both the expansion of the bright core (MFR) and the reconnection of magnetic field surrounding the core can lead to the decrease of the dark cavity in size during the CME propagation outward. Therefore, the zone between the leading edge and the hot channel or filament observed in the EUV passband (*i.e.*, in the early eruption stage or in the low corona) might not totally correspond to the MFR structure.

The existence of a low-density zone between the overlying loops and the hot channel MFR has been displayed clearly through a failed eruption (see Figure 1 of Song et al. 2014b), which demonstrates that the MFR does not occupy all the space below the leading edge in the eruption stage. The low-density zone might be occupied by sheared field lines, different from the overlying loops that are closer to a potential field. During the eruption, the MFR will expand and ascend, and the field lines in the cavity could be transformed into the shell part of the MFR through reconnection occurring in the current sheet beneath the CME (Lin & Forbes 2000; Lin et al. 2004; Zuccarello et al. 2012). The reconnection also injects plasmas into the MFR along the reconnected field lines, and the newly formed shell part of the MFR might possess relatively low or high density depending on the injections and appear as part of the dark cavity or bright core correspondingly. Hence the so-called low-density zone (cavity) could keep existing (Figure 1) or disappear gradually (Figure 3) during the evolution process.

After the CMEs propagate into the high corona (e.g., beyond $2 R_{\odot}$), their cavity might correspond to the MFR totally. We propose one preliminary method to judge the nature of the cavity based on its evolution trend. If the cavity is the MFR, the cavity will continue to expand during the propagation outward and exist for a long time. Eventually it can be detected through the in situ measurements that prove the cavity to be the MFR (Liu et al. 2010; Howard & DeForest 2012). On the other hand, if the cavity is still a low-density zone, its volume might continue to decrease gradually due to the MFR expansion and/or magnetic reconnection (Song et al. 2017; Song et al. 2019). The results in this qualitative study provide one explanation why some CMEs do not exhibit the clear three-part structure (*i.e.*, no obvious cavity) in the high corona. More quantitative analyses and numerical simulations are necessary in the future.

We thank the anonymous referee for the comments and suggestions that helped to improve the original manuscript. We are grateful to Drs. Xin Cheng (NJU), Peng-Fei Chen (NJU), Jun Lin (YNO), Gang Li (UAH), and Bo Li (SDU) for their valuable discussions. We acknowledge the use of data from the *SDO*, *SOHO*, *STEREO*, and *GOES* missions. This work is supported by the Shandong Provincial Natural Science Foundation (JQ201710), the NSFC grants U1731102, U1731101, 41331068, 11790303, and 11790300, and the CAS grants XDA-17040505 and XDA-15010900.

REFERENCES

- Brueckner, G. E., Howard, R. A., Koomen, M. J., et al. 1995, *Sol. Phys.*, 162, 357
- Chen, J. 1996, *J. Geophys. Res.*, 101, 27499
- Chen, P. F. 2009, *ApJ*, 698, L112
- Chen, P. F. 2011, *LRSP*, 8, 1
- Cheng, X., Ding, M. D., Guo, Y., et al. 2014, *ApJ*, 780, 28
- Cheng, X., Li, Y., Wan, L. F., et al. 2018, *ApJ*, 866, 64
- Cheng, X., Zhang, J., Liu, Y., & Ding, M. D. 2011, *ApJ*, 732, L25
- Cheng, X., Zhang, J., Saar, S. H., & Ding, M. D. 2012, *ApJ*, 761, 62
- Del Zanna, G., & Mason, H. E. 2018, *LRSP*, 15, 5
- Forbes, T. G., 2000, *J. Geophys. Res.*, 105, 23153
- Forbes, T. G., Linker, J. A., Chen, J., et al. 2006, *Space Sci. Rev.*, 123, 251
- Forland, B. C., Gibson, S. E., Dove, J. B., Rachmeler, L. A., & Fan, Y. 2013, *Sol. Phys.*, 288, 603
- Gibson, S. E., Foster, D., Burkepile, J., de Toma, G., & Stanger, A. 2006, *ApJ*, 641, 590
- Gopalswamy, N., Shimojo, M., Lu, W., et al. 2003, *ApJ*, 586, 562
- Gosling, J. T., McComas, D. J., Phillips, J. L., & Bame, S. J. 1991, *J. Geophys. Res.*, 96, 7831
- Hayes, A. P., Vourlidas, A., & Howard, R. A., 2001, *ApJ*, 548, 1081
- Howard, T. A., & DeForest, C. E. 2012, *ApJ*, 746, 64
- Howard, T. A., DeForest, C. E., Schneck, U. G., & Alden, C. R. 2017, *ApJ*, 834, 86
- Howard, R. A., Moses, J. D., Vourlidas, A., et al. 2008, *Space Sci. Rev.*, 136, 67

- Illing, R. M. E., & Hundhausen, A. J. 1983, *J. Geophys. Res.*, 88, 10210
- Kippenhahn, R., & Schlüter A. 1957, *ZA*, 43, 36
- Lemen, J. R., Title, A. M., Akin, D. J., et al. 2012, *Sol. Phys.*, 275, 17
- Lin, J., & Forbes, T. G. 2000, *J. Geophys. Res.*, 105, 2375
- Lin, J., Raymond, J. C., & van Ballegoijen, A. A. 2004, *ApJ* 602, 422
- Liu, Y., Davies, J. A., Luhmann, J. G., et al. 2010, *ApJ*, 710, L82
- Liu, Y. D., Luhmann, J. G., Kajdic, P., et al. 2014, *Nature Communications*, 5, 3481
- Liu, Y. D., Zhu, B., & Zhao, X. W. 2019, *ApJ*, 871, 8
- Mikić, Z., & Linker, J. A. 1994, *ApJ*, 430, 898
- Nindos, A., Patsourakos, S., Vourlidas, A., & Tagikas, C. 2015, *ApJ*, 808, 117
- Patsourakos, S., Vourlidas, A., & Stenborg, G. 2013, *ApJ*, 764, 125
- Seaton, D. B., & Darnel, J. M. 2018, *ApJ*, 852, L9
- Song, H. Q., Chen, Y., Zhang, J., et al. 2015, *ApJ*, 808, L15
- Song, H. Q., Cheng, X., Chen, Y. et al., 2017, *ApJ*, 848, 21
- Song, H. Q., Zhang, J., Chen, Y., & Cheng, X. 2014a, *ApJ*, 792, L40
- Song, H. Q., Zhang, J., Cheng, X., et al. 2014b, *ApJ*, 784, 48
- Song, H. Q., Zhang, J., Cheng, X., et al. 2019, *ApJ*, 883, 43
- Veronig, A. M., Podladchikova, T., Dissauer, K., et al. 2018, *ApJ*, 868, 107
- Vourlidas, A., & Howard, R. A. 2006, *ApJ*, 642, 1216
- Vourlidas, A., Lynch, B. J., Howard, R. A., & Li, Y. 2013, *Sol. Phys.*, 284, 179
- Webb, D. F., Forbes, T. G., Aurass, H., et al. 1994, *Sol. Phys.*, 153, 73
- Webb, D. F., & Howard, T. A. 2012, *LRSP*, 9, 3
- Webb, D. F., Lepping, R. P., Burlaga, L. F., et al. 2000, *J. Geophys. Res.*, 105, 27251
- Yan, X. L., Yang, L. H., Xue, Z. K., et al. 2018, *ApJ*, 883, L18
- Zhang, J., Cheng, X., & Ding, M.-D. 2012, *Nature Communications*, 3, 747
- Zhang, J., Dere, K. P., Howard, R. A., & Bothmer, V. 2003, *ApJ*, 582, 520

Zhang, J., Richardson, I. G., Webb, D. F., et al. 2007, *J. Geophys. Res.*, 112, A10102

Zhang, J., Yang, S. H., & Li, T. 2015, *A&A*, 580, A2

Zuccarello, F. P., Bemporad, A., Jacobs, C., et al. 2012, *ApJ*, 744, 66

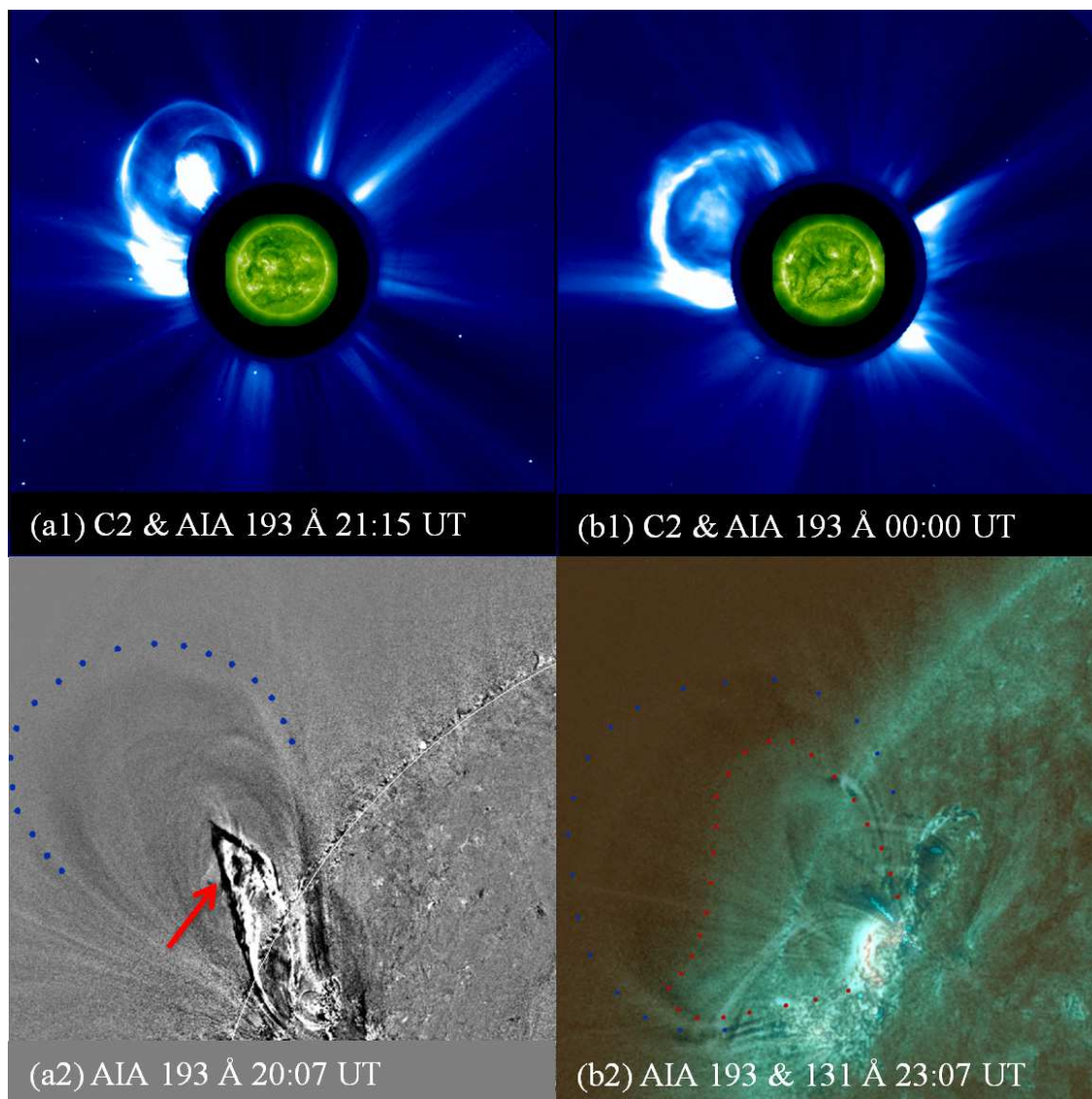


Fig. 1.— Two CMEs with obvious cavity in the coronagraph. Left: The event on 2013 September 24. (a1) The LASCOCO/C2 direct image with the AIA 193 Å image superimposed. (a2) The AIA 193 Å running-difference image, showing the leading edge (blue dots) and the filament as denoted with the red arrow. Right: The event on 2015 February 9. (b1) The LASCOCO/C2 direct image with the AIA 193 Å image superimposed. (b2) The composite image of AIA 193 Å running-difference image (gray) and 131 Å direct image (cyan), showing the leading edge (blue dots) and the hot channel as denoted with the red dots. Panel (a2) is accompanied by an animation that displays the filament eruption process from 19:40 UT to 20:10 UT with a duration of 2 seconds. Panel (b2) is accompanied by the same animation that also displays the hot channel eruption process from 22:50 UT to 23:14 UT. The animation shows the Panel (a2)/(b2) at the left/right side on each frame of the video.

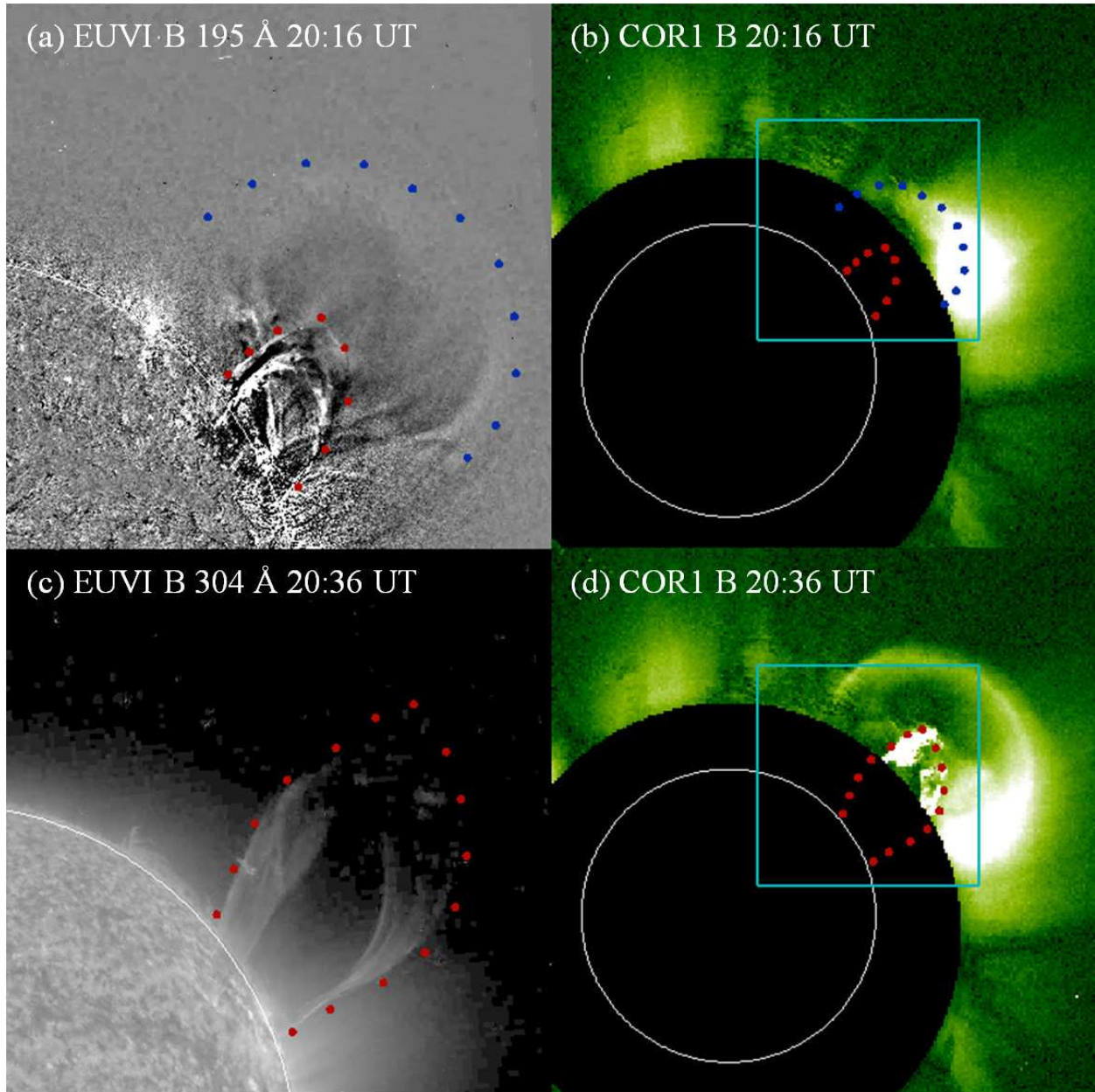


Fig. 2.— Observations of the event on 2013 September 24 by the EUVI B and COR1 B. (a) The running-difference image of EUVI B 195 Å. (b) and (d) The direct images of COR1 B, showing the CME morphology. (c) The direct image of 304 Å. Panel (a) is accompanied by an animation that displays the complete eruption process recorded by the EUVI B. The animation starts at 19:41 UT and ends at 20:26 UT with a duration of 2 seconds.

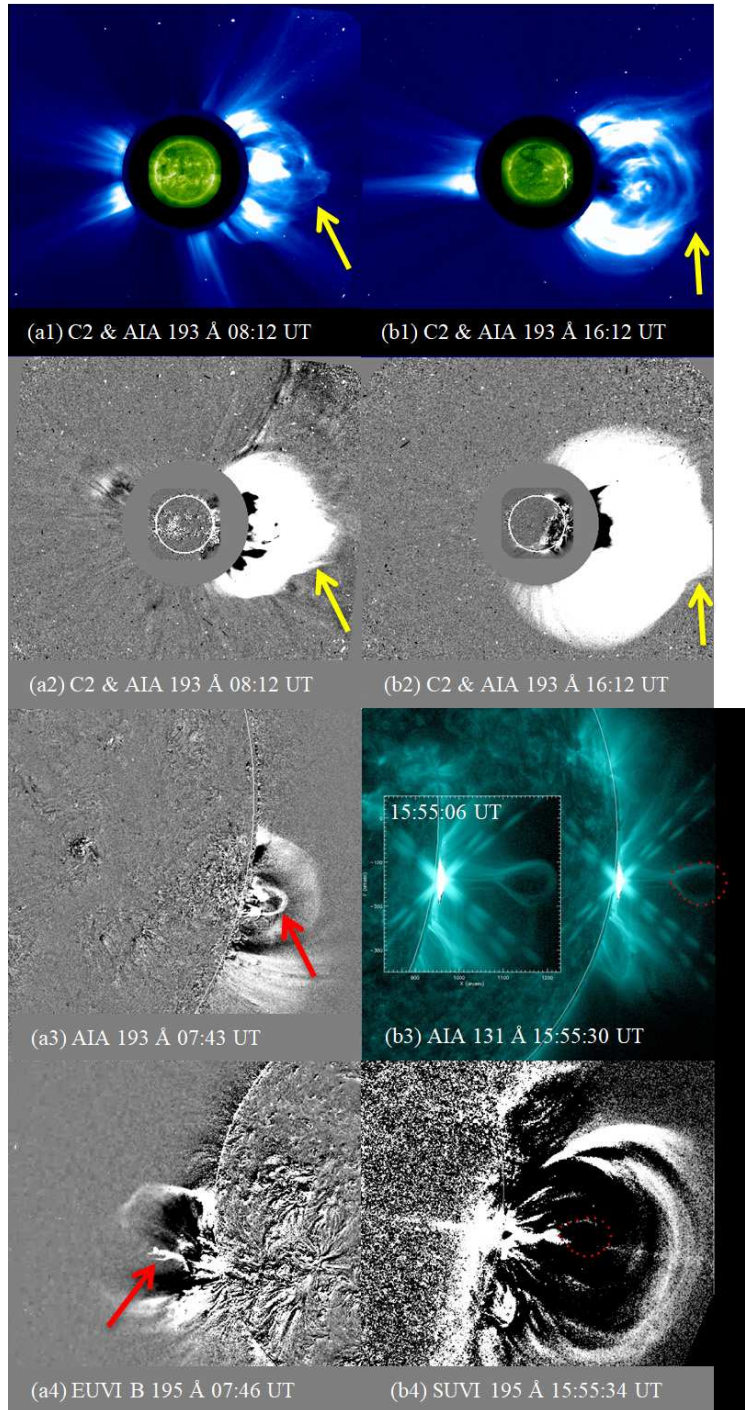


Fig. 3.— Two CMEs without obvious cavity in the coronagraph. Left: The event on 2014 January 6. (a1) The composite image of the LASCO/C2 and AIA 193 Å. (a2)-(a4) The running-difference image of the LASCO/C2, AIA 193 Å, and EUVI B 195 Å, respectively. Right: The event on 2017 September 10. (b1) The composite image of the LASCO/C2 and AIA 193 Å. (b2) The running-difference image of the LASCO/C2. (b3) The direct image of AIA 131 Å. (b4) The running-difference image of the SUVI 195 Å with the 131 Å hot blob outline overplotted.

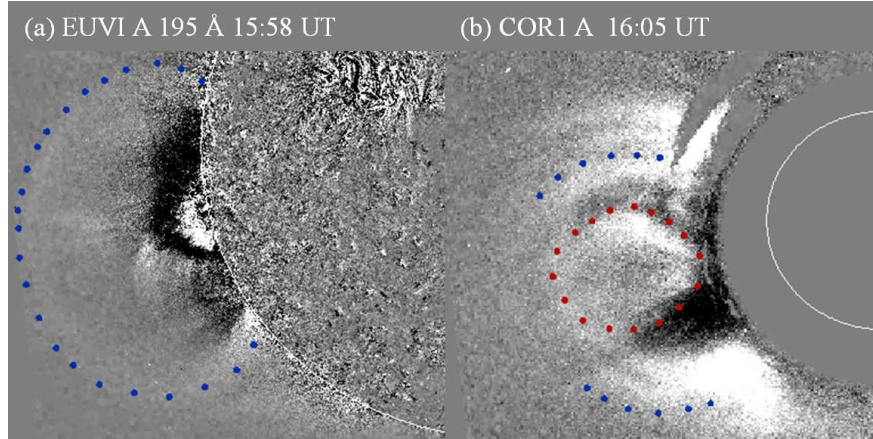


Fig. 4.— The *STEREO-A* observation of the event on 2017 September 10. (a) The running-difference image of EUVI A 195 Å. The blue dots denote the leading front. (b) The running-difference image of COR1 A. The blue and red dots depict the leading edge and the core, respectively. Panel (a) is accompanied by an animation that displays the eruption process from 15:48 UT to 16:10 UT with a duration of 2 seconds. Panel (b) is accompanied by the same animation that displays the eruption process from 15:50 UT to 16:10 UT. The animation shows the Panel (a)/(b) at the left/right side on each frame of the video.

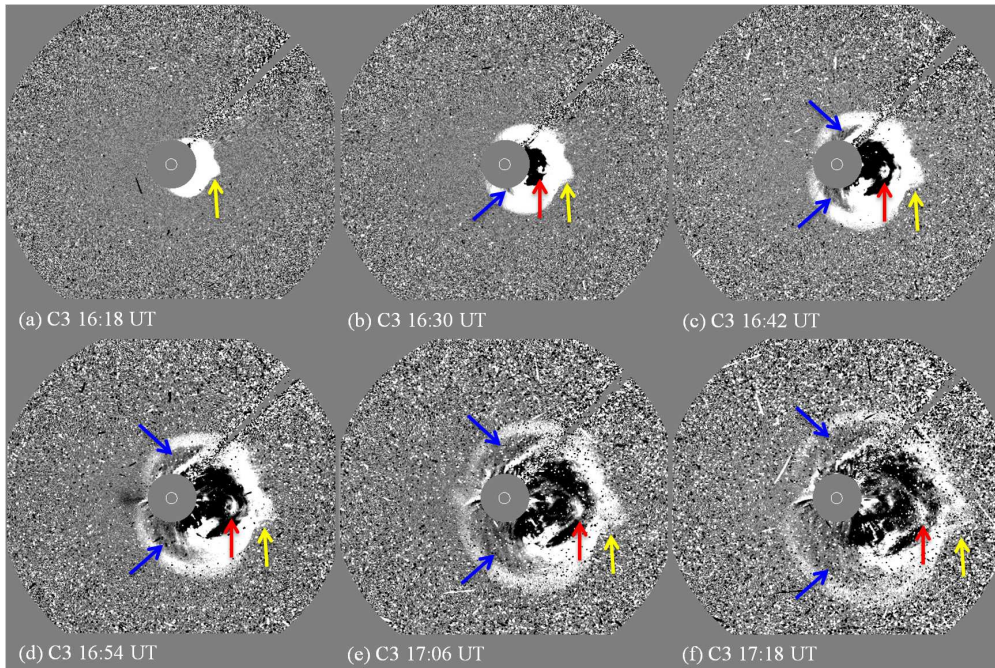


Fig. 5.— The running-difference images of LASCO/C3 on the 20170910 event. The bulge, core, and separation between the shock and the CME front are depicted with the yellow, red, and blue arrows, respectively. The white circle in each panel delineates the solar limb.